JOURNAL OF NANOMATERIALS AND DEVICES
July-Dec 2024, VOL. 2, ISSUE 2, pp. 27-32
https://doi.org/10.61577/jnd.2024.1000012

RESEAPRO JOURNALS

OPEN ACCESS

ORIGINAL ARTICLE

Synthesis and characterization of stannic oxide thin films and their application in quantum dot sensitized solar cells

Vikram P. Bhalekar[1]*, Shivaji M. Sonawane[2], Nilesh S. Kanhe[3], Ashok B. Nawale[4]

[1]Department of Physics, Arts, Science and Commerce College, Rahata, Ahilyanagar
[2]Department of Physics, Bharatiya Jain Sanghatana's A. S. and C College, Wagholi, Pune
[3] Department of Physics, Arts, Commerce and Science College, Satral, Ahilyanagar
[4] Department of Physics, Govt. Vidarbha Institute of Science and Humanities, Amravati

ABSTRACT

The thin films of Stannic Oxide (SnO_2) were deposited on fluorine-doped tin oxide substrates through ambient-modulated Chemical Bath Deposition (CBD). This was done by comparing air and oxygen-bubbled conditions to interpret oxygen's role in phase evolution and defect mitigation. Annealing transformed as deposited (tetragonal with orthorhombic traces) SnO phases into crystalline SnO_2 (mixed tetragonal-orthorhombic), as verified by X-ray diffraction revealing a structural shift. Optical analysis confirmed bandgap widening from ~ 2.0 eV to ~ 3.0 eV with high visible transmittance (> 85%), while scanning electron microscopy revealed granular morphologies influenced by deposition ambient. Quantum-dot-sensitized solar cells fabricated with PbS quantum dots (QDs) and polysulfide electrolyte attaining 0.316 % and 0.787 % power conversion efficiency with CuS and CuSe counter electrode under low-intensity illumination (15 mW cm^{-2}). The low illumination intensity was deliberately chosen to evaluate device behavior under conditions relevant to indoor and low-light applications (an emerging direction for QDSSCs) and to minimize thermal stress and irreversible degradation of the polysulfide electrolyte and PbS layer. The work demonstrates a simple ambient-controlled CBD route for producing functional SnO_2 photoanodes and serves as cost-effective SnO_2-based QDSSCs; further interface engineering will be required to reach competitive efficiencies under full-sun conditions.

KEY WORDS

Chemical bath deposition; Stannic oxide; Quantum dot sensitized solar cells; PbS quantum dots; Polysulphide electrolyte

ARTICLE HISTORY

Received 22 July 2024; Revised 14 September 2024; Accepted 18 September 2024

Introduction

Quantum Dot Sensitized Solar Cells (QDSSCs) are a progression of Dye-Sensitized Solar Cells (DSSCs). By replacing organic dyes with inorganic QDs, it obtains broader spectral absorption and higher theoretical efficiencies through Multiple Exciton Generation (MEG) and hot carrier extraction [1,2]. QDs such as PbS, CdS, and CdSe presents size-dependent tunable bandgaps, aiding absorption from visible to Near-Infrared (NIR) regions and potentially surpassing the Shockley-Queisser limit of ~33% for single-junction cells [3,4]. The typical QDSSC architecture is made up of a wide-bandgap metal oxide photoanode sensitized with QDs, a counter electrode (e.g., CuS or Pt), and a redox electrolyte (e.g., polysulphide for stability with chalcogenide QDs) [2,5]. The photoanode functions as a staging for QD attachment, allowing electron injection from photoexcited QDs into the oxide's conduction band, followed by transport to the Transparent Conductive Oxide (TCO) substrate. Moreover, it is necessary for efficient photoanodes to align high surface area for QD loading, low recombination, and rapid electron transport [2,6].

TiO_2 and ZnO are the widely researched photoanodes in QDSSCs, with TiO_2 mesopores obtaining Power Conversion Efficiencies (PCEs) up to 12% in co-sensitized systems and ZnO nanowires furnishing direct pathways for electron collection [7-9]. However, SnO_2 has gained interest due to its higher bulk electron mobility (100–200 $cm^2\ V^{-1}\ s^{-1}$ compared to TiO_2's 0.1–1 $cm^2\ V^{-1}\ s^{-1}$), larger bandgap (3.6 eV) curtailing UV depletion, and better chemical stability in acidic or polysulphide environments [10-14]. SnO_2 is an n-type semiconductor having a wide bandgap of 3.6 eV at 300 K. It was thus selected for its high electron mobility and stability in QDSSCs [10,12]. CBD was utilized for film deposition on Fluorine-doped Tin Oxide (FTO) glass substrates (sheet resistance 15 Ω/sq). It offered advantages like low-temperature processing (below 100°C), scalability for large-area coatings, and the ability to tune film porosity via bath parameters [13]. Regardless of these merits, SnO_2 has a lower conduction band edge (~0.4 eV below TiO_2), which can lead to slower injection kinetics from certain QDs, and its surface states stimulate recombination, yielding lower open-circuit voltages (Voc) [14,15]. SnO_2 is more commonly employed in DSSCs, where hierarchical or doped structures yield PCEs up to 7–8%, but its application in QDSSCs remains less explored, with reported PCEs typically below 3% due to interface challenges [4,11,14-16].

CBD is a multifunctional, cost-effective method for depositing metal oxide films, allowing precise control over thickness, morphology, and stoichiometry at low temperatures without vacuum equipment [17]. CBD SnO_2 films are usually formed with mixed SnO/SnO_2 phases, necessitating annealing to gain pure rutile SnO_2 [18,19]. Deposition ambient, such as oxygen bubbling, is likely to influence oxygen incorporation, decreasing vacancies that

***Correspondence:** Vikram P. Bhalekar, Department of Physics, Arts, Science and Commerce College, Rahata, India, email: bhalekarvp@gmail.com

function as trap sites [20]. PbS QDs, with bandgaps tunable from 0.4–1.5 eV, work in favor of SnO_2 for electron injection [4,21]. However, optimal SILAR cycles are fundamental to balance coverage and aggregation [21]. Polysulphide electrolytes present stability for sulphide QDs but are likely to corrode SnO_2 surfaces [14]. Earlier works have also stressed the importance of compact layers, surface passivation, counter electrode selection, and performance under low-light conditions [22–24].

In recent years, research has increasingly focused on oxygen-plasma or ambient-oxidation treatments designed to reduce oxygen vacancies in SnO_2 electron-transport layers, on intentional doping of SnO_2 for PbS-based devices, on solid-state PbS–SnO_2 interfaces, and on surface-passivation strategies that effectively suppress recombination [25–31]. High-efficiency liquid-junction QDSSCs have also been realized through optimized counter electrodes and co-sensitization schemes [32,33].

This study examines and evaluates CBD-synthesized SnO_2 thin films under air and oxygen ambient, annealed for phase optimization, and sensitized with PbS QDs via SILAR. Structural, optical, and morphological properties are linked to QDSSC under low-intensity illumination. While SnO_2 photoanodes for QDSSCs are not new, the work highlights the utility of ambient-controlled CBD as a simple route to functional films and situates the incremental advance within the broader context of recent interface-engineering efforts.

Experimental

Materials

All reagents were analytical grade and used as received. sodium stannate trihydrate ($Na_2SnO_3{\cdot}3H_2O$, Sigma-Aldrich ≥ 98%), hydrazine hydrate ($N_2H_4{\cdot}H_2O$, Merck 80%), ammonia solution (NH_4OH, Merck 25%), lead nitrate ($Pb(NO_3)_2$, Merck ≥ 99%), sodium sulphide flakes (Na_2S, Merck ≥ 55%), sulphur powder (S, Merck ≥ 99.5%), sodium hydroxide (NaOH, Merck ≥ 97%), copper sulphate ($CuSO_4{\cdot}5H_2O$, Merck ≥ 99%), sodium thiosulphate ($Na_2S_2O_3{\cdot}5H_2O$, Merck ≥ 99%), and methanol (CH_3OH, Merck ≥ 99.8%). Deionized water (18 MΩ cm) was used throughout. FTO glass substrates (sheet resistance 15 Ω sq^{-1}) were cleaned by sequential ultrasonication in detergent, deionized water, acetone and isopropanol.

Synthesis of SnO_2 thin films

A 0.045 M $Na_2SnO_3{\cdot}3H_2O$ precursor solution was prepared in deionized water. Hydrazine hydrate was added as a complexing agent to impede rapid precipitation and adjusting pH was 10 with addition of NH_4OH dropwise. Cleaned FTO substrates were vertically immersed in the bath maintained at 50°C for 4 hours using a water bath with temperature control (± 1°C). For ambient variation, one deposition was in open air, another with continuous oxygen bubbling (flow rate ~ 50 mL/min) to enhance oxidation and reduce defects [20,24]. Post-deposition, films were withdrawn, ultrasonically cleaned in deionized water for 5 minutes to remove loosely bound particles, and dried at room temperature. Annealing was performed in air at 400°C for 1 h (ramp rate 5°C min^{-1}) to oxidize SnO to SnO_2 and improve crystallinity [18,19].

Synthesis of PbS quantum dots

PbS QDs were deposited on annealed SnO_2 films using the SILAR method, which allows in-situ growth of QDs with good adhesion [14,21]. The process involved alternate immersion in 0.02 M $Pb(NO_3)_2$ (cationic source) and 0.02 M Na_2S (anionic source) aqueous solutions for 30 seconds each at room temperature, followed by rinsing in methanol to remove excess ions and prevent homogeneous precipitation. This cycle was repeated 6 times, determined optimal from prior studies where further cycles lead to aggregation and reduced performance [14,21]. The low concentration and short dip times ensure QD size ~ 5–10 nm, with bandgap ~ 1.3 eV suitable for NIR absorption [4,14].

Characterization techniques

Structural properties were analyzed using an X-ray diffractometer (Bruker D8 Advance, Bruker Corporation, Germany) equipped with Cu Kα radiation (λ = 1.5406 Å), operated over a scan range of 20–80° 2θ with a step size of 0.02°. For Phase Identification Joint Committee on Powder Diffraction Standards (JCPDS) databases was used, crystallite size calculated via Scherrer equation $D = 0.9\lambda / (\beta \cos \theta)$, where β is full width at half maximum (FWHM) [18]. Optical measurements employed UV-Vis-NIR spectrophotometer (JASCO V-670, JASCO Corporation, Japan) in 200–1100 nm range for absorption/transmittance. The band gaps were extracted from Tauc plots $(\alpha h\nu)^2$ vs hν assuming direct transitions [13,15,24]. Morphology was examined by field-emission scanning electron microscopy SEM (FE-SEM; JEOL JSM-7610F, JEOL Ltd., Japan) operated at 15 kV acceleration voltage, the elemental composition was checked with Energy-Dispersive X-Ray Spectroscopy (EDS).

QDSSC fabrication

The sandwich-type cells with an active area of 0.25 cm^2 were assembled with the SnO_2/PbS photoanode. The CuS and CuSe counter electrode prepared by CBD, and a polysulfide electrolyte (1 M Na_2S, 1 M S, 0.1 M NaOH in water/methanol 7:3 v/v) [5,22,34]. Current–voltage characteristics were measured under AM 1.5G illumination attenuated to 15 mW cm^{-2} using a Keithley 2400 source meter. The reduced intensity was selected for two reasons: (i) to assess performance under indoor/low-light conditions that are increasingly relevant for QDSSCs, and (ii) to minimize thermal stress and irreversible degradation of the polysulfide electrolyte and PbS layer that can occur under prolonged full-sun illumination in unoptimized liquid-junction cells. 1-sun (100 mW cm^{-2}) measurements will be reported in subsequent work after interface passivation and doping strategies.

Results and Discussion

Optical properties

The optical characteristics of tin oxide thin films were assessed via UV-Vis-NIR spectroscopy (JASCO UV-Vis-NIR Spectrometer). The optical band gap (Eg) was evaluated using Tauc's relation for direct allowed transitions: $(\alpha h\nu)^2 = A(h\nu - Eg)$, where α is the absorption coefficient, hν is the photon energy, and A is a constant. Extrapolation of the linear region in the Tauc plot to the x-axis yields Eg.

https://doi.org/10.61577/jnd.2024.1000012

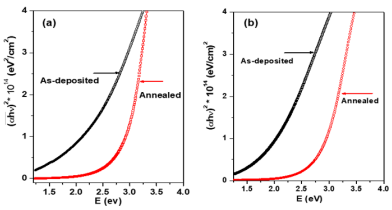

Figure 1. Tauc plots [(αhν)² versus hν] of as-deposited and annealed tin oxide thin films prepared (a) without O_2 bubbling and (b) with continuous O_2 bubbling.

As shown in Figure 1, films deposited without O_2 bubbling exhibited Eg values of 2.20 eV (as-deposited) and 3.00 eV (annealed), whereas those with O_2 bubbling displayed 1.95 eV (as-deposited) and 2.90 eV (annealed). The post-annealing band gap widening is ascribed to the phase transition from SnO (narrower band gap ~ 2.5-3.0 eV) to SnO_2 (wider band gap ~ 3.6 eV in bulk), driven by oxygen incorporation during annealing at 400°C in air. This process increases structural order and decreases sub-band gap defect states, like oxygen vacancies or interstitials, which otherwise facilitate Urbach tail absorption. The slightly lower Eg in O_2-bubbled as-deposited films signifies higher oxygen stoichiometry, potentially introducing donor-like defects that narrow the effective gap.

As presented in Figure 2, annealed films attain > 85% transmittance in the visible spectrum (400-700 nm), significantly greater than as-deposited samples. This improvement stems from improved crystallinity, diminished scattering centers (e.g., grain boundaries and defects), and phase stabilization to SnO_2, which shows low absorption in the visible due to its wide direct band gap. Minor differences between O_2-bubbled and non-bubbled films suggest that deposition oxygen modulates initial defect density. However, annealing homogenizes optical quality, making these films viable as transparent electrodes in photovoltaic devices. Transmittance spectra further delineate the films' viability for optoelectronic applications.

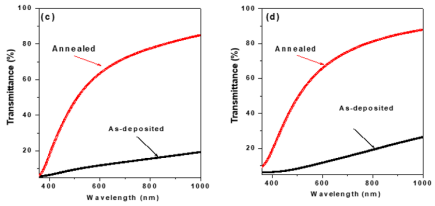

Figure 2. Transmittance spectra (UV–Vis–NIR) of as-deposited and annealed tin oxide thin films deposited (C) without O_2 bubbling and (d) with continuous O_2 bubbling.

Structural properties

Structural evolution was evaluated using X-ray diffraction (XRD; Bruker D8 Advance) with Cu Kα radiation (λ = 1.5406 Å).

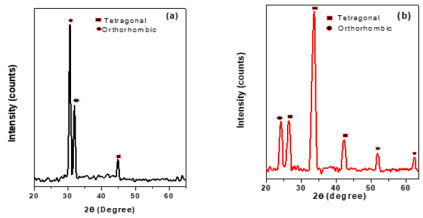

Figure 3. XRD patterns of tin oxide films deposited without O_2 bubbling: (a) as-deposited (polycrystalline SnO, tetragonal + orthorhombic) and (b) annealed at 400°C (phase-pure SnO_2).

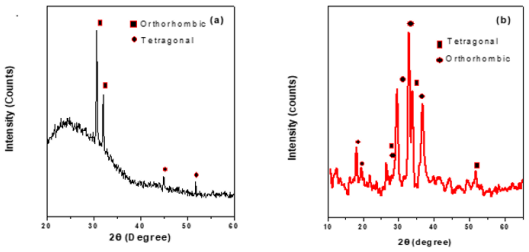

Figure 4. XRD patterns of tin oxide films deposited with continuous O_2 bubbling: (a) as-deposited and (b) annealed at 400°C.

As substantiated by Figures 3(a) and 4(a), as deposited films contain polycrystalline SnO with dominant tetragonal phase (space group P4/nmm) and minor orthorhombic traces (space group Pbcn), indexed to JCPDS Nos. 85-0423 and 72-2324, respectively. Peak positions (e.g., 2θ ≈ 29.8° for (110) tetragonal) corroborates phase purity without extraneous impurities. Post-annealing (Figures 3(b) and 4(b)), spectra exhibit sharp peaks corresponding to SnO_2 (JCPDS No. 41-1445 for tetragonal rutile, space group P42/mnm; and traces of orthorhombic, JCPDS No. 78-1063), with no residual SnO or secondary phases, indicating complete oxidation:

$$2SnO + O_2 \rightarrow 2SnO_2$$

Scherrer analysis of peak broadening (e.g., (110) at 2θ ≈ 26.6°) uncovers crystallite sizes enhancing from ~10-15 nm (as-deposited) to ~ 20-30 nm (annealed), reflecting thermal-induced grain coalescence.

The structural homology between O_2-bubbled and non-bubbled films post-annealing accentuates that O_2 bubbling primarily impacts precursor oxidation kinetics without altering final stoichiometry. This phase purity and crystallinity are required for minimizing trap states in charge transport applications.

The observed band gap variations correlate with this transition, as thin-film SnO_2 Eg (2.9-3.0 eV) deviates from bulk (3.6 eV) due to defect-induced states and residual strain from nanoscale grains.

Surface morphology

Surface topography was characterized by scanning electron microscopy (SEM; JEOL model).

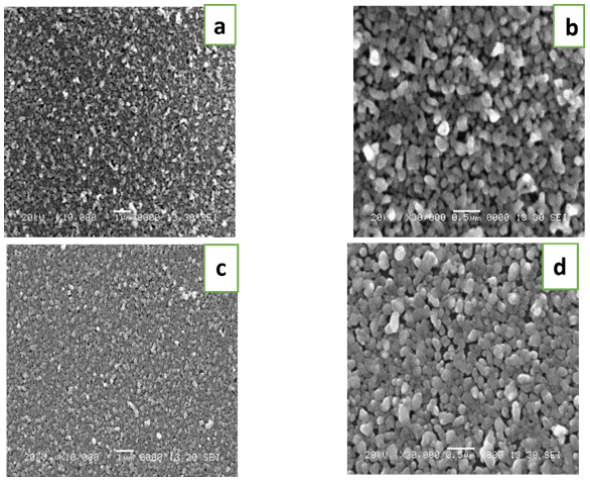

Figure 5. SEM micrographs of films deposited without O_2 bubbling: (a,b) as-deposited and (c,d) annealed, showing uniform granular morphology and grain growth after annealing.

https://doi.org/10.61577/jnd.2024.1000012

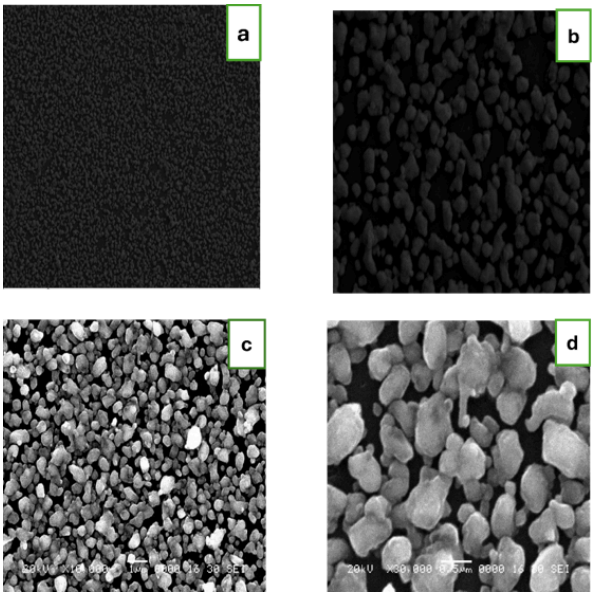

Figure 6. SEM micrographs of films deposited with continuous O_2 bubbling: (a,b) as-deposited and (c,d) annealed, illustrating granular morphology with occasional voids.

Figures 5(a,b) and 6(a,b) depict as-deposited films with uniform, dense granular morphology, particle sizes 50-100 nm. Annealing (Figures 5(c,d) and 6(c,d)) promotes Ostwald ripening, yielding larger grains (150-300nm) and enhanced compactness, reducing porosity and improving inter-particle connectivity.

Non-O_2-bubbled annealed films show superior surface coverage, likely due to homogeneous nucleation, whereas O2-bubbled counterparts exhibit partial voids, attributable to gas-induced disruption of adatom diffusion during deposition (Figures 5 and 6). This morphology is related to XRD crystallinity, larger grains reduce boundary scattering, advances electron mobility (μe ~10-50 $cm^2/V{\cdot}s$ for SnO_2). For surface-sensitive applications such as gas sensing, larger O_2-bubbled particles increase active area, while compact non-bubbled films favor conductivity in electrodes. The deposition and annealing significantly modulate properties, with SnO-to-SnO_2 conversion optimizing band gap, transmittance, and order for optoelectronics.

Application in QDSSCs

In QDSSCs, the photoanode band gap has a decisive role in overall device performance. A wider band gap increases visible-light transparency, decreases parasitic absorption by the oxide itself, and enables the QDs to dominate photon harvesting across the visible and NIR regions. This promotes efficient exciton generation within the QDs while the photoanode facilitates rapid electron extraction, thereby suppressing recombination losses. The annealed SnO_2 film deposited without oxygen bubbling (Eg ≈ 3.00 eV, Figure 1) was selected as the photoanode. Although slightly lower than bulk rutile SnO_2 (3.6 eV), the value is typical of thin-film material and still provides enough transparency. The film blends > 85 % visible transmittance, compact granular morphology that assists higher electron mobility, and phase-pure SnO_2 validated by XRD (Figures 2, 3 and 5). These characteristics collectively calibrate light management and reduces defect-related losses in the QDSSC architecture.

Photovoltaic performance

QDSSC devices were fabricated using the annealed non-O_2-bubbled SnO_2 photoanode sensitized with PbS QDs, paired with CuS and CuSe counter electrodes in polysulfide electrolyte. J-V characteristics were observed under simulated solar illumination (AM 1.5G, 15 mW/cm^2).

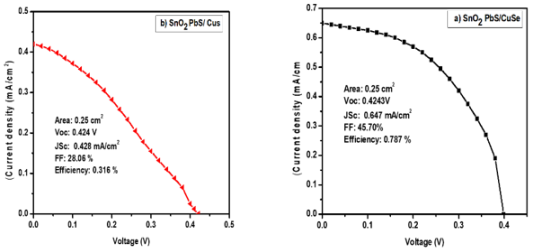

Figure 7. J–V characteristics of QDSSCs employing the annealed non-O_2-bubbled SnO_2 photoanode sensitized with PbS QDs, measured under 15 mW cm^{-2} illumination with CuS and CuSe counter electrodes.

Figure 7 uncovers the typical sigmoidal J–V curves. The CuSe-based device presents a steeper slope near short-circuit and a higher fill factor, showing superior overall performance compared with the CuS counterpart.

Performance metrics are tabulated below (Table 1).

Table 1. SnO_2-based QDSSCs's photovoltaic parameters with CuS and CuSe counter electrodes.

Sample	Area cm^2	Voc (V)	Jsc (mA/cm^2)	FF (%)	Efficiency (%)
SnO_2/CuS	0.25	0.424	0.428	28	0.316
SnO_2/CuSe	0.25	0.42	0.647	45.70	0.787

The higher efficiency of the CuSe device (0.787 %) originates from its superior electrocatalytic activity towards the S_x^{2-}/S^{2-} redox couple, which lessens charge-transfer resistance at the counter electrode and reduces recombination. The modest open-circuit voltages (≈ 0.42 V) are assigned to residual interface recombination at the SnO_2/PbS and SnO_2/electrolyte interfaces, a consequence of SnO_2's relatively low-lying conduction-band edge and the absence of a passivation layer. The fill-factor values (28 % for CuS, 45.7 % for CuSe) portray series-resistance contributions from granular boundaries and contact interfaces (visible in SEM, Figure 5) in addition to limited shunt resistance caused by occasional pinholes. Nevertheless, the gained efficiencies (0.316 % and 0.787 %) underscores that ambient-controlled CBD SnO_2 can function as a viable, low-cost photoanode for PbS-QDSSCs under low-intensity illumination, with CuSe emerging as the more effective counter electrode.

Discussion

The ambient-modulated CBD process followed by mild annealing produces phase-pure, highly transparent SnO_2 films whose morphological features can be tuned by the presence or absence of continuous oxygen bubbling. The observed band-gap widening (≈ 2.0 eV to ≈ 3.0 eV) and crystallite growth are consistent with the elimination of oxygen-vacancy-related defect states, a conclusion supported by recent oxygen-plasma and ambient-oxidation studies on SnO_2 electron-transport layers [25,26]. Device efficiencies remain modest, as expected for a non-passivated SnO_2/PbS interface. The lower conduction-band

https://doi.org/10.61577/jnd.2024.1000012

edge of SnO_2 relative to TiO_2 and the absence of a blocking or passivation layer facilitate recombination, limiting Voc to ~ 0.42 V. The superior performance of the CuSe counter electrode is attributed to its higher electrocatalytic activity toward the polysulfide redox couple, which lowers charge-transfer resistance at the counter-electrode/electrolyte interface. These observations align with recent reports that emphasize counter-electrode selection and interface passivation as critical levers for improving liquid-junction QDSSCs [22,30–33].

To place the present results in a broader context, Table 2 compares key performance metrics of the devices reported herein with those of selected previously published SnO_2- and PbS-based QDSSCs.

Table 2. Comparative performance of selected SnO_2- and PbS-based quantum-dot-sensitized solar cells.

Photoanode /Sensitizer	Counter electrode	Illumination intensity	PCE (%)	Voc (V)	Reference /Year
SnO_2 / CdS–CdSe	Pt	100 mW cm^{-2}	1.8–2.5	0.45 –0.55	[4]
SnO_2 / PbS	CuS	100 mW cm^{-2}	< 1.0	≈ 0.40	[6]
Hierarchical SnO_2 / PbS	Cu_2S	100 mW cm^{-2}	≈ 1.5	0.48	[14]
TiO_2 / PbS (passivated)	CuS	Artificial light	> 5	0.55	[24]
SnO_2 (ambient-CBD) / PbS	CuS	15 mW cm^{-2}	0.316	0.424	This work
SnO_2 (ambient-CBD) / PbS	CuSe	15 mW cm^{-2}	0.787	0.42	This work

Table 2 highlights that, the PCEs obtained in the present study under low-intensity illumination are competitive with early SnO_2/PbS devices measured under full-sun conditions, especially when the reduced photon flux is taken into account. Second, the clear advantage of CuSe over CuS mirrors trends reported for other chalcogenide counter electrodes. Third, the table underscores that the highest efficiencies in the literature have been achieved only after the introduction of hierarchical morphologies, doping or surface-passivation layers strategies that remain to be implemented in the present ambient-controlled CBD system. The deliberate use of low-intensity illumination (15 mW cm^{-2}) allows evaluation under conditions relevant to indoor photovoltaics and reduces thermal degradation of the electrolyte and QD layer.

Overall, ambient-controlled CBD offers a scalable, low-cost and experimentally straightforward route to functional SnO_2 photoanodes. The present results constitute a proof-of-concept demonstration; competitive efficiencies which require the interface-engineering approaches already shown to be effective in higher-performance SnO_2 and PbS based devices [27–33].

Conclusion

SnO_2 thin films were formed by ambient-modulated chemical bath deposition and converted into phase-pure SnO_2 through controlled annealing (at 400°C) successfully. The non-oxygen-bubbled films, characterized by a band gap of ≈ 3.0 eV, high visible transmittance (> 85 %), and compact morphology, were sensitized with PbS QDs and utilized as photoanodes in QDSSCs. The devices under 15 mW cm^{-2} illumination provided power-conversion efficiencies of 0.316 % for CuS and 0.787 % CuSe counter electrode. The superior performance of the CuSe counter electrode is attributed to its enhanced electrocatalytic activity. The overall modest efficiencies originate mainly from interfacial recombination associated with residual surface defects and the absence of a passivation layer.

The work establishes ambient-controlled CBD as a simple and cost-effective method for producing functional SnO_2 photoanodes suitable for low-light QDSSC applications. Future improvements will focus on surface passivation, doping and full-sun characterization to raise device performance toward literature benchmarks.

References

1. Tian J, Cao G. Semiconductor quantum dot-sensitized solar cells. Nano Rev. 2013;4(1):22578. https://doi.org/10.3402/nano.v4i0.22578
2. Ballabio M, Cánovas E. Electron transfer at quantum dot–metal oxide interfaces for solar energy conversion. ACS Nanosci Au. 2022;2(5):367. https://doi.org/10.1021/acsnanoscienceau.2c00015
3. O'regan B, Grätzel M. A low-cost, high-efficiency solar cell based on dye-sensitized colloidal TiO_2 films. Nature. 1991;353(6346):737-740. https://doi.org/10.1038/353737a0
4. Hossain MA, Jennings JR, Koh ZY, Wang Q. Carrier generation and collection in CdS/CdSe-sensitized SnO_2 solar cells exhibiting unprecedented photocurrent densities. ACS Nano. 2011;5(4):3172-3181. https://doi.org/10.1021/nn200315b
5. Chung NT, Nguyen PT, Tung HT, Phuc DH. Quantum dot sensitized solar cell: photoanodes, counter electrodes, and electrolytes. Molecules. 2021;26(9):2638. https://doi.org/10.3390/molecules26092638
6. Huang Q, Li F, Gong Y, Luo J, Yang S, Luo Y, et al. Recombination in SnO_2-based quantum dots sensitized solar cells: the role of surface states. J Phys Chem C. 2013;117(21):10965-10973. https://doi.org/10.1021/jp402601v
7. Chou TP, Zhang Q, Fryxell GE, Cao GZ. Hierarchically structured ZnO film for dye-sensitized solar cells with enhanced energy conversion efficiency. Adv Mater. 2007;19(18):2588-2592. https://doi.org/10.1002/adma.200602927
8. Hosono E, Fujihara S, Kakiuchi K, Imai H. Growth of submicrometer-scale rectangular parallelepiped rutile TiO_2 films in aqueous $TiCl_3$ solutions under hydrothermal conditions. J Am Chem Soc. 2004;126(25):7790-7791. https://doi.org/10.1021/ja048820p
9. Rakgalakane BP, Sikhwivhilu LM, Moloto MJ, van Wyk J, Moloto N. Effect of the propanol–water volume ratios on the properties of SnO_2 nanocrystals. Mater Res Express. 2015;2(1):015012. https://doi.org/10.1088/2053-1591/2/1/015012
10. Huu NK, Son DY, Jang IH, Lee CR, Park NG. Hierarchical SnO_2 nanoparticle-ZnO nanorod photoanode for improving transport and life time of photoinjected electrons in dye-sensitized solar cell. ACS Appl Mater Interfaces. 2013;5(3):1038-1043. https://doi.org/10.1021/am302729v

https://doi.org/10.61577/jnd.2024.1000012

11. Li X, Yu Q, Yu C, Huang Y, Li R, Wang J, et al. Zinc-doped SnO_2 nanocrystals as photoanode materials for highly efficient dye-sensitized solar cells. J Mater Chem A. 2015;3(15):8076-8082. https://doi.org/10.1039/c5ta01176k
12. Batzill M, Diebold U. The surface and materials science of tin oxide. Prog Surf Sci. 2005;79(2-4):47-154. https://doi.org/10.1016/j.progsurf.2005.09.002
13. Ikhmayies SJ, Ahmad-Bitar RN. An investigation of the bandgap and Urbach tail of vacuum-evaporated SnO_2 thin films. Renew Energy. 2013;49:143-146. https://doi.org/10.1016/j.renene.2012.01.045
14. Chen S, Wang Y, Li Y, Lin J, Zhang X. $BaSnO_3$-SnO_2 heterojunction mesoporous photoanode for quantum dot-sensitized solar cells. Mater Res Bull. 2023;167:112431. https://doi.org/10.1016/j.materresbull.2023.112431
15. Qian J, Liu P, Xiao Y, Jiang Y, Cao Y, Ai X, et al. TiO_2-coated multilayered SnO_2 hollow microspheres for dye-sensitized solar cells. Adv Mater. 2009;21(36):3663-3667. https://doi.org/10.1002/adma.200900525
16. Milan R, Selopal GS, Epifani M, Natile MM, Sberveglieri G, Vomiero A, et al. ZnO@ SnO_2 engineered composite photoanodes for dye sensitized solar cells. Sci Rep. 2015;5(1):14523. https://doi.org/10.1038/srep14523
17. Khallaf H, Chai G, Lupan O, Heinrich H, Park S, Schulte A, et al. Investigation of chemical bath deposition of ZnO thin films using six different complexing agents. J Phys D: Appl Phys. 2009;42(13):135304. https://doi.org/10.1088/0022-3727/42/13/135304
18. Al-Saadi TM, Kamil ZA. Study the effect of manganese ion doping on the size-strain of SnO_2 nanoparticles using X-ray diffraction data. Ibn al-Haitham J Pure Appl Sci. 2023;36(3):158-166. https://doi.org/10.30526/36.3.3052
19. Cai FS, Wang J, Yuan ZH, Duan YQ. SnO_2 nanosheet as a photoanode interfacial layer for dye-sensitized solar cells. Optoelectron Lett. 2011;7(5):321-324. https://doi.org/10.1007/s11801-011-1025-8
20. Rus SF, Ward TZ, Herklotz A. Strain-induced optical band gap variation of SnO_2 films. Thin Solid Films. 2016;615:103-106. https://doi.org/10.1016/j.tsf.2016.06.057
21. Bhalekar VP, Rajendra Prasad MB, Supekar AT. Impact of number of sensitizer SILAR cycles on the performance of ZnO based PbS quantum dot-sensitized solar cells. J Mater Sci: Mater Electron. 2023;34(31):2083. https://doi.org/10.1007/s10854-023-11456-w
22. Kumar PN, Kolay A, Kumar SK, Patra P, Aphale A, Srivastava AK, et al. Counter electrode impact on quantum dot solar cell efficiencies. ACS Appl Mater Interfaces. 2016;8(41):27688-27700. https://doi.org/10.1021/acsami.6b08921
23. Bi Z, Zhang S, Thandapani M, Zhu Y, Zheng Y, Liem NQ, et al. High shunt resistance SnO_2-PbO electron transport layer for perovskite solar cells used in low lighting applications. Adv Sustain Syst. 2021;5(11):2100120. https://doi.org/10.1002/adsu.202100120
24. Bhalekar VP, Baviskar PK, Prasad R, Palve BM, Kadam VS, Pathan HM. PbS sensitized TiO_2 based quantum dot solar cells with efficiency greater than 5% under artificial light: effect of compact layer and surface passivation. Eng Sci. 2019;7(2):38-42. https://doi.org/10.30919/es8d676
25. Won JH, Han SH, Park BK, Chung TM, Han JH. Effect of oxygen source on the various properties of SnO2 thin films deposited by plasma-enhanced atomic layer deposition. Coatings. 2020;10(7):692. https://doi.org/10.3390/coatings10070692
26. Li J, Li L, Chen W, Yi Q, Zou G. Room-temperature processed high-quality SnO_2 films by oxygen plasma activated e-beam evaporation. Nanotechnology. 2021;32(2):025606. https://doi.org/10.1088/1361-6528/abbce9
27. Jia T, Sun C, Shi N, Yu D, Long F, Hu J, et al. Efficient oxygen vacancy defect engineering for enhancing visible-light photocatalytic performance over SnO_{2-} x ultrafine nanocrystals. Nanomaterials. 2022;12(19):3342. https://doi.org/10.3390/nano12193342
28. Wang L, Wang H, Jia Y, Wang Y, Kubo T, Liu Y, et al. Dip-Coated SnO_2 Electron Transport Layer for Efficient and Stable PbS Quantum Dot Photovoltaics. Solar RRL. 2022;6(10):2200488. https://doi.org/10.1002/solr.202200488
29. Hoang Huy VP, Nguyen TM, Bark CW. Recent advances of doped SnO_2 as electron transport layer for high-performance perovskite solar cells. Materials. 2023;16(18):6170. https://doi.org/10.3390/ma16186170
30. Kar A, Sain S, Rossouw D, Knappett BR, Pradhan SK, Wheatley AE. Facile synthesis of SnO_2–PbS nanocomposites with controlled structure for applications in photocatalysis. Nanoscale. 2016;8(5):2727-2739. https://doi.org/10.1039/c5nr07036h
31. Hori K, Zhang Y, Tusamalee P, Nakazawa N, Yoshihara Y, Wang R, et al. Interface passivation effects on the photovoltaic performance of quantum dot sensitized inverse opal TiO_2 solar cells. Nanomaterials. 2018;8(7):460. https://doi.org/10.3390/nano8070460
32. Prasittichai C, Hupp JT. Surface modification of SnO_2 photoelectrodes in dye-sensitized solar cells: significant improvements in photovoltage via $Al2O_3$ atomic layer deposition. J Phys Chem Lett. 2010;1(10):1611-1615. https://doi.org/10.1021/jz100361f
33. Halder G, Ghosh D, Ali MY, Sahasrabudhe A, Bhattacharyya S. Interface engineering in quantum-dot-sensitized solar cells. Langmuir. 2018;34(35):10197-10216. https://doi.org/10.1021/acs.langmuir.8b00293
34. Palve BM, Kadam VS, Jagtap CV, Jadkar SR, Pathan HM. A simple chemical route to synthesis the CuSe and CuS counter electrodes for titanium oxide based quantum dot solar cells. J Mater Sci: Mater Electron. 2017;28(19):14394-14401. https://doi.org/10.1007/s10854-017-7300-0

https://doi.org/10.61577/jnd.2024.1000012